Article:
Liu, K., Qiu, R., Zhou, P. et al. (2025) Geotextile-encased cinder gravel columns: a coupled DEM-FDM analysis. Geosynthetics International, 32 (2). pp. 302-317. ISSN: 1072-6349

https://doi.org/10.1680/jgein.23.00161

Geotextile-Encased Cinder Gravel Columns: A Coupled DEM-FDM Analysis

Author 1

- **Kaiwen Liu**, Associate Professor; Email: kaiwen.liu@queensu.ca
- School of Civil Engineering, Southwest Jiaotong University, Chengdu 610031, China
- MOE Key Laboratory of High-Speed Railway Engineering, Southwest Jiaotong University, Chengdu 610031, China

Author 2

- **Ruizhe Qiu**, PhD Candidate; Email: qiuruizhe@my.swjtu.edu.cn
- School of Civil Engineering, Southwest Jiaotong University, Chengdu 610031, China

Author 3

- **Pengfei Zhou**, Junior Engineer; Email: 136880746@qq.com
- Guangzhou Metro Design and Research Institute Co., Ltd., Guangzhou 510499, China

Author 4

- **Tengfei Wang***, Associate Professor; Email: w@swjtu.edu.cn
- School of Civil Engineering, Southwest Jiaotong University, Chengdu 610031, China
- MOE Key Laboratory of High-Speed Railway Engineering, Southwest Jiaotong University, Chengdu 610031, China (*Corresponding author)
- ORCID: 0000-0003-4079-0687

Author 5

- **David P. Connolly**, Professor; Email: D.Connolly@leeds.ac.uk
- School of Civil Engineering, University of Leeds, Leeds LS2 9JT, UK

Author 6

- **Jian Xiao**, Master's Candidate; Email: 2744876189@qq.com
- School of Civil Engineering, Southwest Jiaotong University, Chengdu 610031, China

Tengfei Wang*, Ph.D., Associate Professor

School of Civil Engineering, Southwest Jiaotong University, Chengdu 610031, China
MOE Key Laboratory of High-Speed Railway Engineering, Southwest Jiaotong University, Chengdu 610031, China (*Corresponding author)
ORCID: 0000-0003-4079-0687; Email: w@swjtu.edu.cn

Abstract

Cinder gravel, a porous, lightweight, and durable volcanic byproduct, has the potential to be a sustainable and cost-effective alternative to conventional stone columns for ground improvement applications. Its use in soft soils, however, requires sufficient confining pressure to prevent bulging and thus performance degradation. Geotextile-encased cinder gravel (GECG) columns are therefore an innovate method to overcome this, however their bearing response and pressure-deformation characteristics have received limited study. This paper presents a comprehensive numerical analysis for GECG columns using a coupled discrete element and finite difference method (DEM-FDM). The hybrid DEM-FDM framework enables the simulation of individual particle behavior while maintaining efficiency in modeling continuous, homogeneous materials. The key novelties are examining the macro and mesoscopic behavior of GECG columns under triaxial compression. To do so, the development of the numerical model is introduced, followed by its validation and calibration against triaxial test results. Subsequently, a parametric analysis of GECG columns investigates the influence of relative density and gradation on the compression behavior and load capacity. Upon triaxial compression, the findings reveal a significant radial expansion near the column top, with stress and deformation fields aligning with the column's bearing capacity. The relative density exerts limited influence on the geotextile's radial deformation, and the higher content of coarse particles in the gradation enhanced the bearing capacity of the GECG columns.

***Keywords*:** geosynthetics; ground improvement; cinder gravel; stone column; DEM-FDM; triaxial test

NOTATIONS

Basic SI units are shown in parentheses

E_c	Contact effective modulus (Pa)
k_n	Normal stiffness (Pa)
k_s	Tangential stiffness (Pa)
μ	Interparticle friction coefficient (dimensionless)
n	Porosity (dimensionless)
σ_3	Confining pressure (Pa)
E_{50}	Secant modulus (Pa)
φ	Apparent friction angle (°)
c	Apparent cohesion (Pa)
ε_1	Axial strain (dimensionless)
q	Deviatoric stress (Pa)
p	Mean stress (Pa)
E_s	Young's modulus for shell element (Pa)
E_{sc}	Effective contact modulus (Pa)
v	Poisson's ratio (dimensionless)
d_{60}	Size such that 60% of particles are finer than this size (m)
d_{30}	Size such that 30% of particles are finer than this size (m)
d_{10}	Size such that 10% of particles are finer than this size (m)
C_u	Coefficient of uniformity (dimensionless)
C_c	Coefficient of curvature (dimensionless)

ABBREVIATIONS

CFG	Cement-Fly ash-Gravel
ESC	Encased Stone Columns
GECG	Geotextile-Encased Cinder Gravel
DEM-FDM	Discrete Element and Finite Difference Method

1. Introduction

As urbanization accelerates and transportation networks expand, traversing weak soil regions becomes an inevitable aspect of transportation infrastructure (Nguyen et al., 2023b; Wang et al., 2022). Soft soils are typically characterized by low bearing capacity, high compressibility, low permeability, and gradual post-construction settlement, meaning ground improvement is crucial before constructing embankments on such weak foundations (Baral et al., 2021). Experience from high-speed railway and highway construction (Feng et al., 2024) shows that geosynthetic-reinforced and column-supported embankments (Nguyen et al., 2023a) are an effective solution for soft ground improvement (Wang et al., 2023b). Common column types within this structure include stone columns, deep mixing columns (Wang et al., 2023a), jet grout columns (Connolly et al., 2020), cement-fly ash-gravel (CFG) piles (Liu et al., 2023), unreinforced concrete piles (Ma et al., 2021), and reinforced concrete piles. Stone columns, composed of granular material, provide vertical drainage channels within their voids, granting them high permeability and accelerating primary consolidation of the ground soil, thus quickly mitigating post-construction embankment settlement (Liu et al., 2024). Using granular materials such as crushed stones for piling circumvents the use of cement as often required for other pile types. This avoids cement production-related atmospheric pollution and prevents secondary pollution from cement leaching into the soil and groundwater. Cost estimation (Huang, 2011) illustrates a comparative advantage of stone columns over deep mixing columns for geosynthetic-reinforced and column-supported embankments. Specifically, the expenditure per kilometer for stone columns registers at only 58% of the total for CFG pile, and a mere 44% of that for prestressed concrete pile.

Cinder gravel, or scoria, is a sustainable and eco-friendly fill material gaining attention in transportation infrastructure (Hearn et al., 2019). As a volcanic byproduct, this porous, lightweight, and durable material offers numerous engineering benefits for transportation (Luo et al., 2020). Utilizing cinder gravel as fill material promotes resource conservation and waste reduction while minimizing some environmental impacts associated with traditional construction materials (Wang et al., 2021). When crafted into specialized stone columns, cinder gravel's unique properties, such as high permeability, low density, and excellent drainage characteristics, make it well-suited for embankments, subgrades, and other foundation elements within transport infrastructure. Furthermore, using cinder gravel columns to support embankments can potentially reduce greenhouse gas emissions and energy consumption related to conventional material extraction, processing, and transportation. Although cinder gravel columns possess numerous advantages, for very soft soils they require adequate

54 confining pressure from the surrounding soil. If not then column bulging may occur, making them unsuitable
55 for improving soft clayey ground with undrained shear strength values below 15 kPa (Kempfert and Raithel,
56 2005).
57
58 Encasing stone columns with suitable materials is an established solution for providing the extra
59 confinement needed to prevent excessive column bulging (Pandey et al., 2022). A multitude of experimental,
60 analytical, and numerical studies have investigated the behavior of soft clay enhanced with encased stone
61 columns (ESC) (Gu et al., 2016; Pandey et al., 2021; Rajesh, 2017; Zhang et al., 2021). For example, Hong et
62 al. (2016) explored the response of encased stone columns, observing that bulging profiles depend on the
63 properties of the encasement material (Miranda et al., 2015). Alternatively, Ou Yang et al. (2017) examined the
64 stress and deformation characteristics of soft clay reinforced with ESC, while Gu et al. (2017a) studied porosities
65 and contact-force distribution changes within geogrid-encased stone columns using the discrete element
66 method. Miranda et al. (2017) assessed the influence of geotextile encasement on soft soil reinforced with fully
67 penetrating stone columns, discovering that encased columns supported 1.7 times the vertical stress of ordinary
68 columns. Castro (2017) evaluated the performance of ESC groups, identifying column length and arrangement
69 as crucial factors affecting performance. Yoo and Abbas (2019) investigated the performance of geosynthetic-
70 encased stone columns in soft clay under vertical cyclic loading, observing more significant benefits under cyclic
71 loading than static loading.
72
73 Chen et al. (2021) examined the impact of encasement stiffness on geosynthetic-encased stone column-
74 supported embankment performance over soft clay, observing significant improvements in settlement reduction,
75 stress concentration ratio, and excess pore water pressure dissipation. Xu et al. (2021) explored the stress-
76 strain behavior of uncased and geogrid-encased stone columns, suggesting short columns penetrate soft soil
77 even under minor stress and that encasement increases bearing capacity by 3-6 times, depending on geogrid
78 stiffness. Zhang et al. (2020) analyzed geosynthetic-encased stone column performance under vertical cyclic
79 loading, considering the influence of loading parameters and column dimensions on stress distribution,
80 settlement, excess pore water pressure, and column bulging. Considering these studies, most have focused on
81 the response of ESC under uniaxial compression, without exploring ESC behavior under triaxial compression.
82
83 This study investigates a novel application involving the incorporation of cinder gravel waste as the

aggregate within geosynthetic-encased columns. The primary objective is to investigate the compressive behavior of geotextile-encased cinder gravel (GECG) columns to evaluate their potential for ground improvement. Initially, the stress and deformation characteristics of encased cinder gravel specimens subjected to triaxial compression are simulated using a coupled DEM-FDM model, with calibration of meso- and macro-parameters based on triaxial testing. Subsequently, the bearing capacity of GECG columns, particularly those with higher length-to-diameter ratios, is examined, and the mesoscopic behaviors of the encased cinder gravel assemblies are analyzed. Finally, the implications for the practical design of GECG columns are elucidated through a parametric study, considering two influential factors: the relative density and the gradation of cinder gravels.

2. Modeling of Triaxial Tests

This section delineates the application of DEM simulation (Cui et al., 2024) to cinder gravel assemblies and the construction of a coupled DEM-FDM model for encased cinder gravels. An exhaustive model development narrative is presented, with pertinent macroscopic and mesoscopic parameters calibrated based on triaxial test results, considering stress-strain relations, failure lines, radial and axial strain, and column deformation patterns. The effectiveness of the coupled DEM-FDM methodology is validated for both macroscopic and mesoscopic encased specimen analysis. In both DEM and DEM-FDM models, the average ratio of unbalanced force was 10^{-5}, while the gravity acceleration equated to 9.8 m/s².

2.1 DEM Simulation of Cinder Gravel Assemblies

2.1.1 Specifications of Cinder Gravel

Cinder gravel, a lightweight aggregate comprising volcanic cinders, is sometimes employed as a fill material in construction. Its excellent drainage, high porosity, and low-density characteristics render it a useful solution for filling voids and stabilizing structures. Additionally, the material is easily transportable and rapidly layered, thereby establishing a stable foundation for transport infrastructure and other structures. Adhering to guideline JGJ 79-2012 (Ministry of Housing and Urban-Rural Development of the PRC, 2013), the grain size of stone column fills must range between 20−150 mm. To ensure precise testing, a triaxial test apparatus's dimensions must maintain a specimen diameter to maximum grain size ratio exceeding 5:1. Hence, the analysis focused on cinder gravels with grain sizes smaller than 15 mm. Figure 1 shows the cinder gravels' gradation under analysis, where the coefficient of uniformity and curvature were 3.00 and 1.64, respectively. Modified Proctor

compaction tests resulted in maximum and minimum dry densities of 1.09 and 0.89 g/cm^3, respectively, for the cinder gravel specimens.

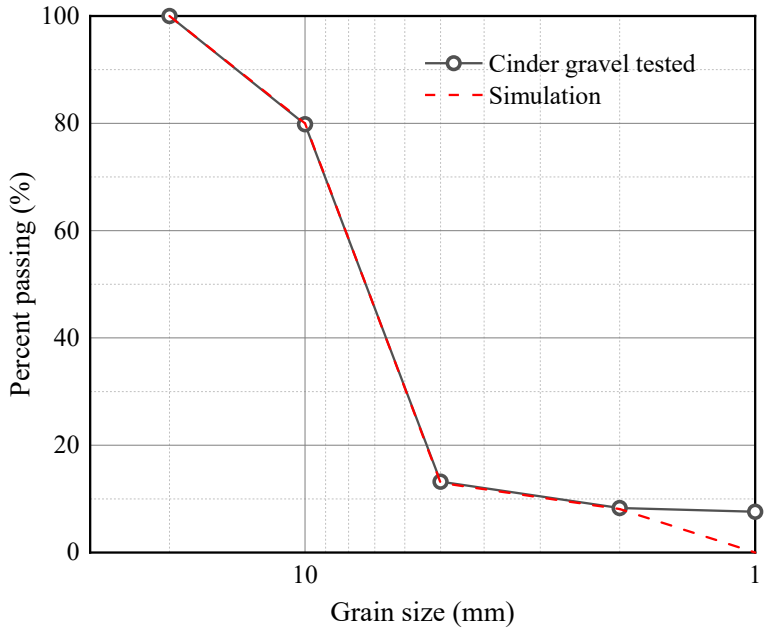

Figure 1. Particle size distribution

2.1.2 Summary of Laboratory Tests

A medium-sized triaxial apparatus was employed to conduct consolidated drained triaxial tests on cinder gravel, encased by geotextile with sample dimensions of 100 mm diameter and 200 mm height. The resultant stress-strain relations of the specimens were obtained, with a consideration of shear strength variations under different confining pressures and relative densities. Additionally, employing digital image measurements allowed for the non-contact real-time detection of radial strain in the specimen throughout the triaxial compression test procedure. Focus is laid upon the peak stress, failure strain, apparent cohesion, friction angle, and circumferential deformation of the specimen. This elucidates the load deformation characteristics of the cinder gravels with and without geotextile encasement.

The properties of the cinder gravel samples are as described in Section 2.1.1. The experimental design encompasses three sets: the triaxial compression test of cinder gravel without encasement, and the triaxial compression tests of the GECG column under two relative densities. All test samples were maintained in a dry state. The triaxial apparatus has a maximum axial load of 200 kN, a maximum confining pressure of 3.0 MPa, and a maximum axial shear strain of 20%. The specimens of different groups were subjected to confining pressures of 50, 100, and 150 kPa respectively. The protocol for the consolidated drained triaxial compression

tests follows the ASTM D7181-20 specification. For encased specimens, a latex membrane was adhered to the inner surface of the sample mold, followed by a geotextile layer. The cinder gravel was then introduced in a layered fashion. Upon completion of specimen installation, black markings were added at the 0.25 H, 0.5 H, and 0.75 H positions on the rubber membrane (H denotes the specimen height), serving as detection points for subsequent camera inspection of specimen deformation patterns.

2.1.3 Numerical Model Development

This section is to build the numerical model to replicate the triaxial test, and then calibration is performed in Sec 2.1.4.

Based on the particle size distribution shown in Figure 1, the initial soil gradation was adjusted and grouped into four categories, as depicted in Figure 2. To enhance computational efficiency while maintaining model accuracy, particles smaller than 1.0 mm were assigned to the 1.0 to 2.0 mm size group.

The DEM model, constructed to the dimensions of the experimental apparatus (Figure 2), measured 200 mm in height and 100 mm in diameter. Two rigid square walls were positioned at the top and bottom of the cinder gravel assemblies. A radially oriented cylindrical wall was employed to apply confining pressure via servo-control. The radius expansion method governed the ball generation process, and the linear contact model was used for simulating inter-particle interactions of cohesionless soils. Adhering to the experimental procedure in Sec 2.1.2, the upper wall remained static, while the lower wall gradually ascended at a rate of 6×10^{-7} m/s to impose a compressive force on the specimen. Simultaneously, real-time measurements of displacements for the upper and lower walls, as well as their respective average stresses, were documented throughout the loading phase.

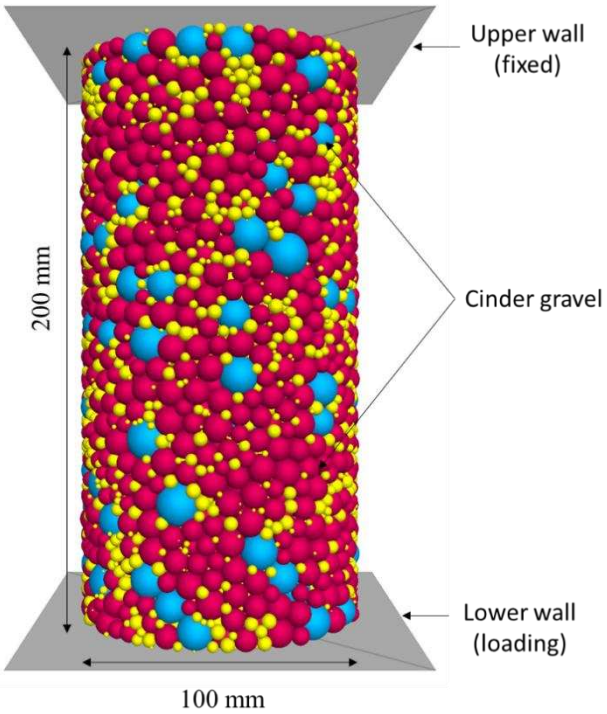

Figure 2. DEM schematic of cinder gravel assemblies in triaxial tests

2.1.4 Model Calibration

The numerical model was used to compute stress-strain relationships under various confining pressures, and compared with the experimental data. Following trials and a parametric analysis, the model parameters were adjusted to yield satisfactory curves, validated against experimental data (Figure 3). Simulated and experimental results displayed strong correlation at confining pressures of 50, 100, and 150 kPa. The specimen exhibited a linear stress increase with strain during the shearing initial stage. Upon attaining peak stress (shear strength), however, the specimen demonstrated strain-hardening behavior, maintaining near-stable shear stress as strain further intensified. Table 1 encompasses additional technical parameters pertinent to the cinder gravels. These parameters were determined through a well-accepted trial-and-error method, widely used for micro parameters calibration (Qu et al., 2019; Jia et al., 2018; Wang et al., 2014; Cai et al., 2007; Bai et al., 2022). To further ensure accuracy, a rigorous process involving sensitivity analysis, regularized analysis, regression function, and artificial neural network (Qu et al., 2019) was followed. Genetic algorithm also employed to speed up the determination of the precise micro parameters. The strong correlation between simulated and experimental outcomes under confining pressures of 50, 100, and 150 kPa, as depicted in Figure 3, attests to the efficacy of the chosen parameters. Table 2 shows the comparison of cinder gravel parameters between the test and numerical simulation. These parameters revealed that the apparent friction angle and secant modulus

of simulated granular materials closely aligned with the experimental findings, thus giving confidence in the numerical model's ability to simulating triaxial tests.

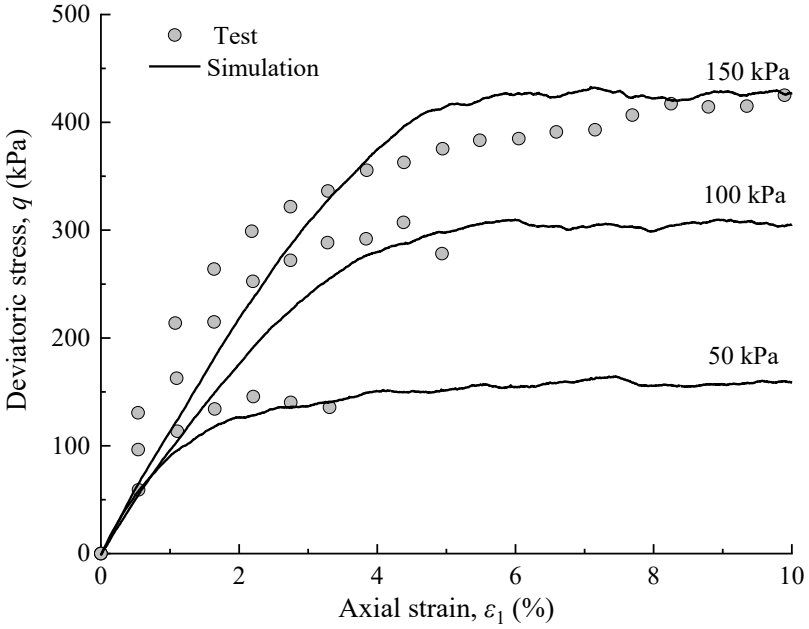

Figure 3. Stress-strain comparison: laboratory tests vs. numerical simulation

Table 1. Parameters for cinder gravel assemblies at the mesoscopic scale

Parameter	Symbol and unit	Value
Contact effective modulus	E_c (kPa)	7×10^6
Normal-to-tangential stiffness ratio	k_n / k_s	3.5
Interparticle friction coefficient	μ	0.8
Porosity	n	0.4
Number of particles	—	54 410

Table 2. Parameter comparison - laboratory test vs. numerical simulation

Parameter	Test	Numerical model
Confining pressure, σ_3 (kPa)	50–150	50–150
Porosity, n	0.4	0.4
Secant modulus, E_{50} (MPa)	10.9–14.6	9.4–12.1
Apparent friction angle, φ (°)	36.4	36.5
Apparent cohesion, c (kPa)	2.1	0.5

2.2 Coupled DEM-FDM Modeling of Encased Cinder Gravel

2.2.1 Numerical Model development

DEM is used to model granular and particulate materials, simulating individual particles and interactions, thereby excelling in microscale phenomena. Conversely, FDM solves partial differential equations governing continuum mechanics, making it useful for macroscale analysis. Coupling the two approaches allows for the simulation of both microscale and macroscale behavior, thus providing understandings of material behavior under diverse conditions. The synthesis capitalizes on each method's strengths while minimizing their individual limitations.

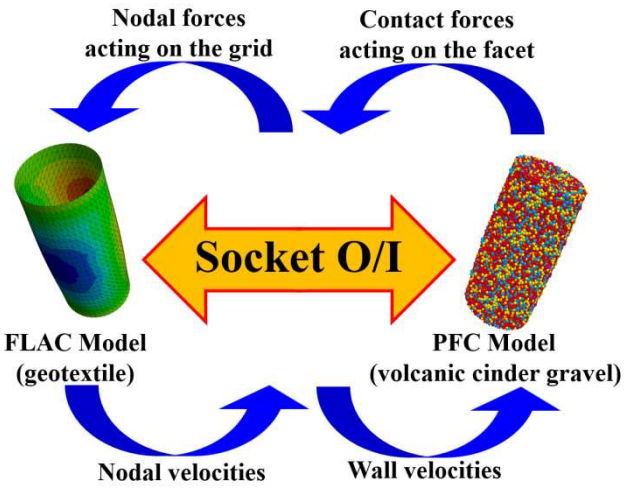

Figure 4. Data transfer scheme in the coupled DEM-FDM model

Figure 4 shows the data transfer scheme in coupled DEM-FDM model. The coupling logic's working principle integrates contact forces and torques with wall surfaces, determining an equivalent force system on the shell vertices. These forces transmit to adjacent nodes through specified stiffness values. Furthermore, force

and displacement transfer adhere to Newton's second law and the force-displacement criterion, prompting structural elements to update. These updates modify geometric parameters and structural element stiffness, ensuring numerical stability. In essence, the wall elements facilitate particle contact force and displacement transmission to shell elements, with both experiencing forces and deformations collectively. Consequently, the equivalent force and displacement transfer system, based on shell and wall elements, enables frictional interaction simulation between geotechnical fabric and particles in the shear direction by establishing particle-wall contact.

The present study executed this fusion using PFC3D and FLAC3D software packages (Tan et al., 2021). Figure 5 presents the development of an encased cinder gravel model for DEM-FDM triaxial tests. The column specimen, with a height of 200 mm and a diameter of 100 mm, concurrently generated a geotextile sleeve with a 100 mm diameter, wherein cinder gravel particles, produced according to the experiment's gradation, formed a spherical assembly. The mesoscopic parameters of the cinder gravel particles are listed in Table 1 through triaxial tests. The mechanical and physical properties of the geosynthetics used in this study are in accordance with reference (Liu et al., 2022). In this paper, the geotextile's elastic modulus was acquired from narrow strip tensile tests as shown in Figure 6 and the results were summarized in Table 3. The Poisson's ratio for geotextile was obtain from the literature as 0.3 (Kadhim et al., 2018; Keykhosropur et al., 2012; Debnath and Dey, 2017). The geotextile sleeve, modelled by shell structure elements, was simplified by using a linearly elastic model mainly incorporating its elastic deformations as widely did in numerical simulations (Tizpa et al., 2023; Tan et al., 2021; Hamad et al., 2016; Mohapatra et al., 2017; Kadhim et al., 2018). Table 4 summarized the mesoscopic parameters of coupled DEM-FDM numerical simulations. The terms "Interparticle friction coefficient" was determined using a trial-and-error approach within the bounds defined by Abu-Farsakh et al. (2007). In terms of contact, linear contacts were established between cinder gravel and geotextile (ball-wall). Configuring contact effective modulus, normal-to-tangential stiffness ratio, and interparticle friction coefficient enabled geotextile-particle frictional interaction simulation. The terms "Contact effective modulus" and "Normal-to-tangential stiffness ratio" refer to the contact parameters between the ball and the facet. These two parameters are essential for the data exchange between FLAC3D and PFC3D and are integral to the coupling computations as outlined by Qu et al. (2019). The values were derived through iterative experimentation based on particle attributes, as supported by Jia et al. (2018), to prevent particle escape from the boundary.

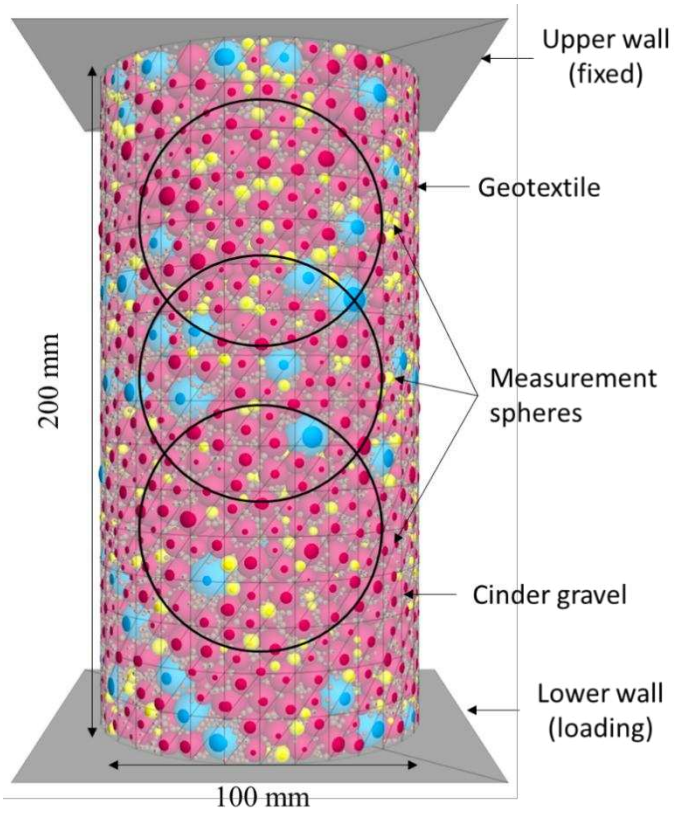

226

227 Figure 5. Schematic of encased cinder gravel in DEM-FDM triaxial tests

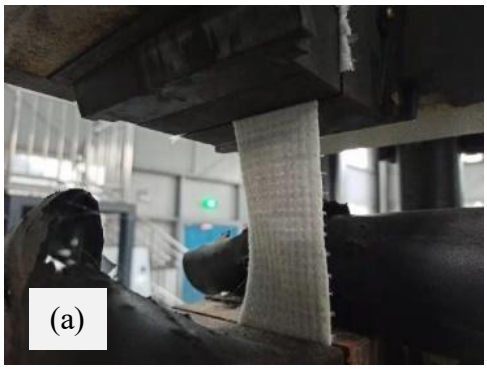

228

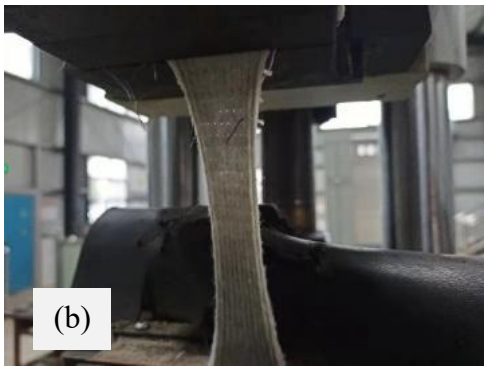

229

230 Figure 6. Narrow strip tensile test for geotextile: (a) before destruction; (b) after destruction

231 Table 3. Tensile properties of geotextile material

Strain	Tensile strength
2% Elongation	2.3 kN/m
4% Elongation	4.6 kN/m
6% Elongation	6.9 kN/m
8% Elongation	9.2 kN/m

Table 4. Mesoscopic parameters for coupled DEM-FDM simulations

Parameter	Symbol and unit	Value
Young's modulus for shell element	E_s (Pa)	1.15×10^7
Poisson's ratio	v	0.3
Contact effective modulus	E_{sc} (Pa)	7×10^7
Normal-to-tangential stiffness ratio	k_n / k_s	0.01
Interparticle friction coefficient	μ	0.8

Model construction was divided into three stages:

(1) The first stage involved the generation of particles and geotextile sleeves, including the creation of the continuous shell structure elements and walls. In accordance with triaxial tests, square walls are placed horizontally above and below the particle assembly for the shearing particles, while a cylindrical wall of identical geometry and dimensions was generated circumferentially using the wall-structure command.Subsequently, employing a radius expansion method, spherical particles with a porosity of 0.2 were generated within the geotextile sleeve according to a predetermined gradation, followed by initial equilibrium calculations to eliminate unbalanced forces.

(2) The second stage was the consolidation phase. It involved a self-coded fish language (adaptable to the software) that applied a confining pressure directly to the geotextile sleeve shell elements, increasing the confining pressure at a rate of 10 kPa per 200 time-steps until reaching a defined value.

(3) The third stage was the shearing phase. It entailed the upper wall remaining stationary, while the lower wall compressed the specimen at a rate of 6×10^{-7} m/s.

The displacement and average stress of the upper and lower walls was recorded in real-time throughout. A measuring sphere is a virtual spherical object used to calculate various mechanical properties of a granular material being simulated. It is typically placed within the simulation domain and used to measure the vertical and radial stresses, particle contact forces, porosity, and coordination numbers. The measuring spheres chosen had diameters of 80 mm, with measurement positions at the upper, middle, and lower sections. Each measuring sphere containing no fewer than 2,000 particles.

2.2.2 Model Calibration

Under varying confining pressures, the stress-strain curves obtained from the numerical model of triaxial tests on Encased cinder gravels were compared with the results of laboratory tests. These are shown in Figure 7a, where the deviatoric stress refers to the normal stress on the base rigid wall. Throughout the shearing process, the stress-strain curves exhibited strong agreement with the laboratory triaxial results. During the initial phase of shearing, the stress in the numerical model increased rapidly due to the volumetric shrinkage of the cinder gravel assembles. This is more pronounced at higher pressures, as the gravel assembly behaves more like a rigid body. Subsequently, the stress under different confining pressures increased linearly with axial strain, maintaining a constant value after reaching peak stress. As illustrated in the p-q failure plane (Figure 7b), the numerical simulation results aligned well with laboratory test outcomes, yielding an apparent friction angle of 36.3° and an apparent cohesion of 143.5 kPa for the Encased cinder gravels. These were close to the laboratory results. The secant modulus obtained from the stress-strain curves also aligned well under different confining pressures. The macroscopic and microscopic parameters of the tests and numerical simulations are compared in Table 5.

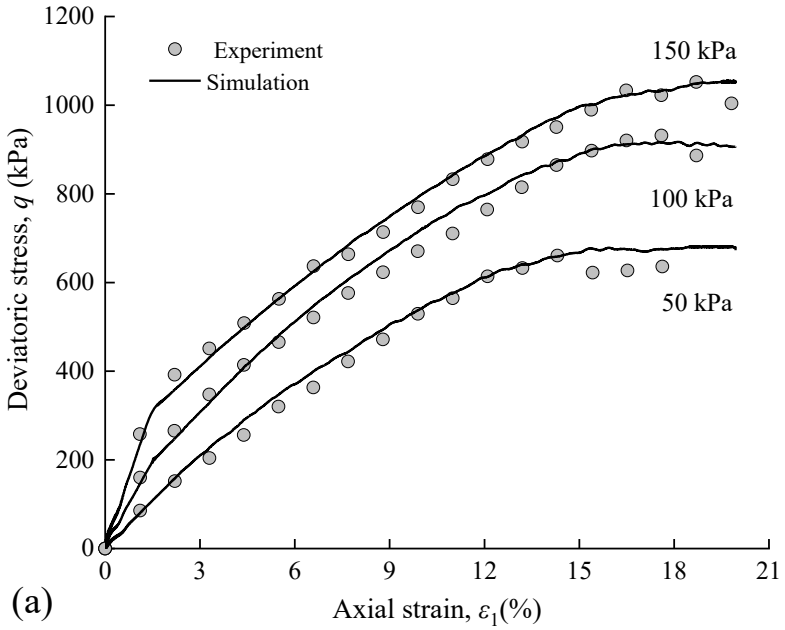

(a)

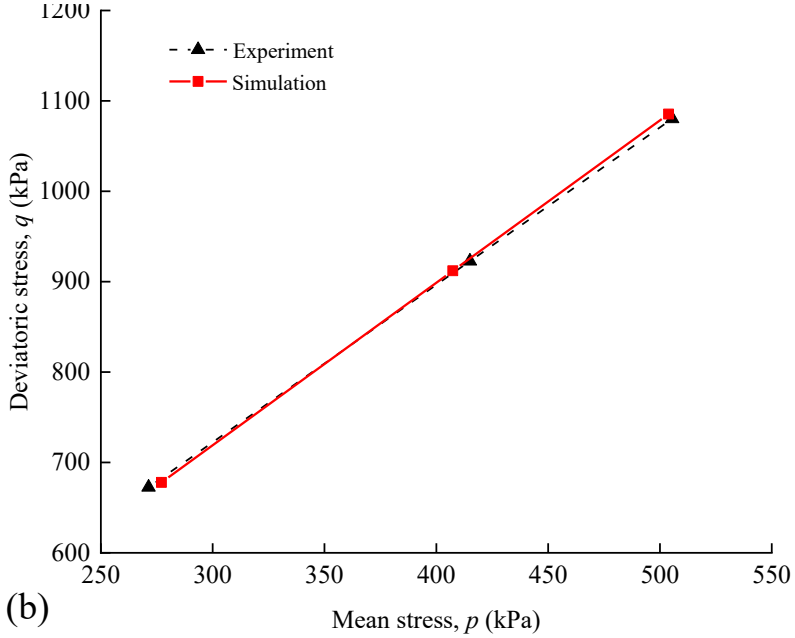

Figure 7. Stress-strain relations (a) and failure lines (b) in p−q stress plane

Table 5. Parameter comparison: laboratory test vs. numerical simulation for specimens

Parameter	Test	Numerical model
Confining pressure, σ_3 (kPa)	50–150	50–150
Porosity, n	0.4	0.4
Secant modulus, E_{50} (MPa)	5.7–10.9	6.4–10.8
Apparent friction angle, φ (°)	36.8	36.3
Apparent cohesion, c (kPa)	153.8	143.5

To ascertain the accuracy of simulating geotextile (continuous medium) deformation within the numerical model, the radial deformation of the geotextile at heights of 0.25H, 0.5H, and 0.75H within the specimen (H representing the total column height) was examined and compared to radial deformation derived from experimental digital measurement techniques. As depicted in Figure 8, the numerical model and laboratory model tests exhibited similar maximum expansion quantities and expansion tendencies under various confining pressures. Under a confining pressure of 50 kPa (Figure 8a), initial shearing revealed expansion at various heights increased linearly with the augmentation of axial strain. Further, the rate of volumetric expansion incrementally accelerated with the accumulation of axial strain. The maximum axial strains corresponding to radial strains at 0.75H, 0.5H, and 0.25H were 18.0%, 13.1%, and 7.4%, respectively. Under a confining pressure of 100 kPa (Figure 8b), the maximum axial strains corresponding to radial strains at 0.75H, 0.5H, and 0.25H were 13.6%, 10.1%, and 4.2%, respectively. Under a confining pressure of 150 kPa (Figure 8c), the maximum axial strains corresponding to radial strains at 0.75H, 0.5H, and 0.25H were 14.2%, 10.5%, and 3.6%, respectively. In conclusion, the expansion deformation patterns under varying confining pressure demonstrated consistency and aligned with the laboratory results.

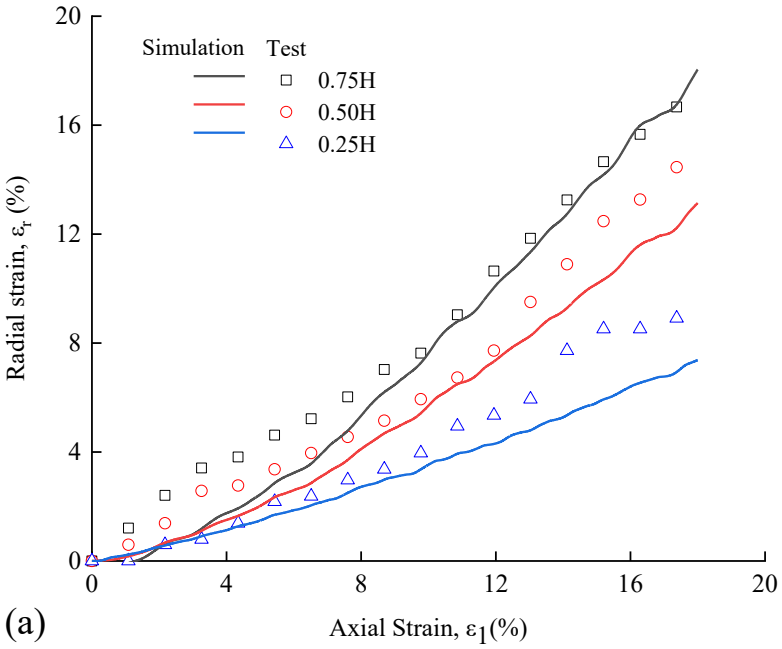
Simulation
Test
0.75H
0.50H
0.25H
Radial strain, ε_r (%)
Axial Strain, ε_1(%)
0
4
8
12
16
20

(a)

287

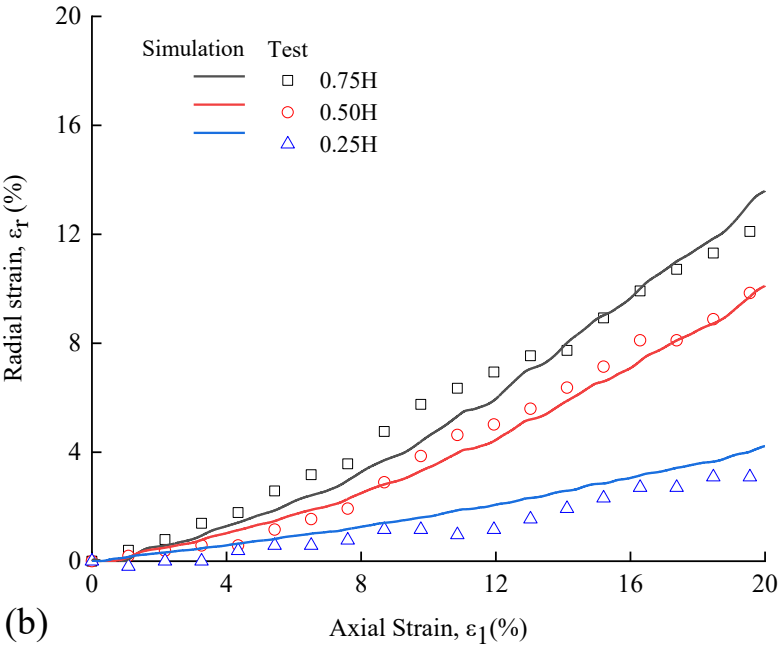
Simulation
Test
0.75H
0.50H
0.25H
Radial strain, ε_r (%)
Axial Strain, ε_1(%)
0
4
8
12
16
20

(b)

288

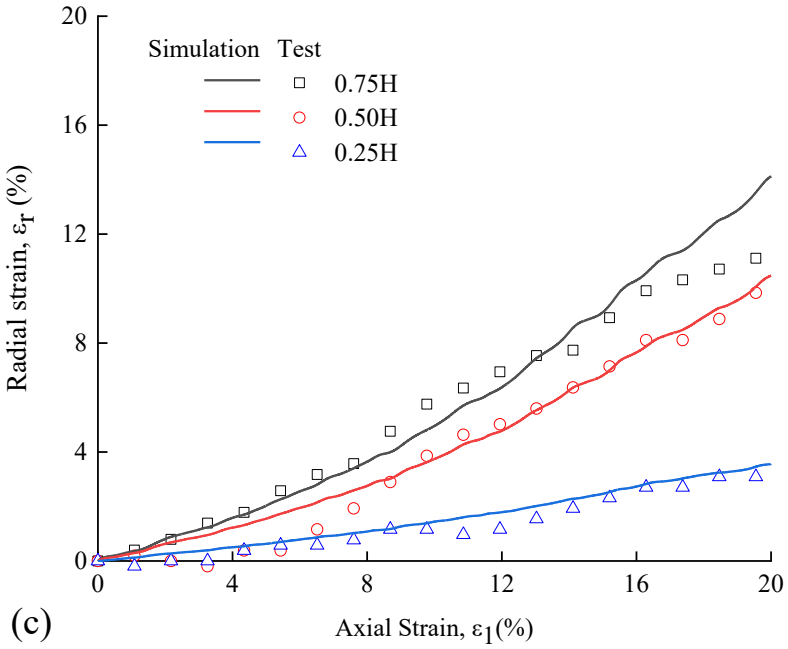

Figure 8. Radial and axial strain relationships at varying confining pressures: (a) 50 kPa; (b) 100 kPa; (c) 150 kPa (H is the specimen height)

Figure 9 compares the triaxial test results with the numerical model outcomes under confining pressures of 50, 100, and 150 kPa. The left section of Figure 9 presents full-surface photographs of the specimens before and after shearing, captured using digital measurement technology. Due to the constraining influence of the lower rigid wall and the upper geotextile on the expansion deformation of the cinder gravel particles, a distinctly convex upper portion and a smaller middle-to-lower region were evident in the post-shear specimen. The right section of Figure 9 shows the displacement contours of encased specimens in the numerical model after shearing. To maintain consistency with the lab experiment, the radial deformation of the geotextile was restrained at the upper and lower ends within the numerical model. Notably, the deformed specimen shape from the numerical model corresponded to that of the laboratory experiment, with the maximum expansion at various heights being consistent in terms of magnitude. Moreover, a discontinuous displacement gradient is discernible through the internal particle displacement contour (numerical model), with substantial shear deformation concentrated in relatively narrow, band-like areas, and borders that are nearly parallel, constituting distinct shear bands. The deformation of specimens under different confining pressures consistently exhibited a convex upper portion and a smaller middle-to-lower region, with shear bands appearing among internal particles. As the confining pressure increased, the specimen's upper convexity and the radial deformation of the geotextile diminished.

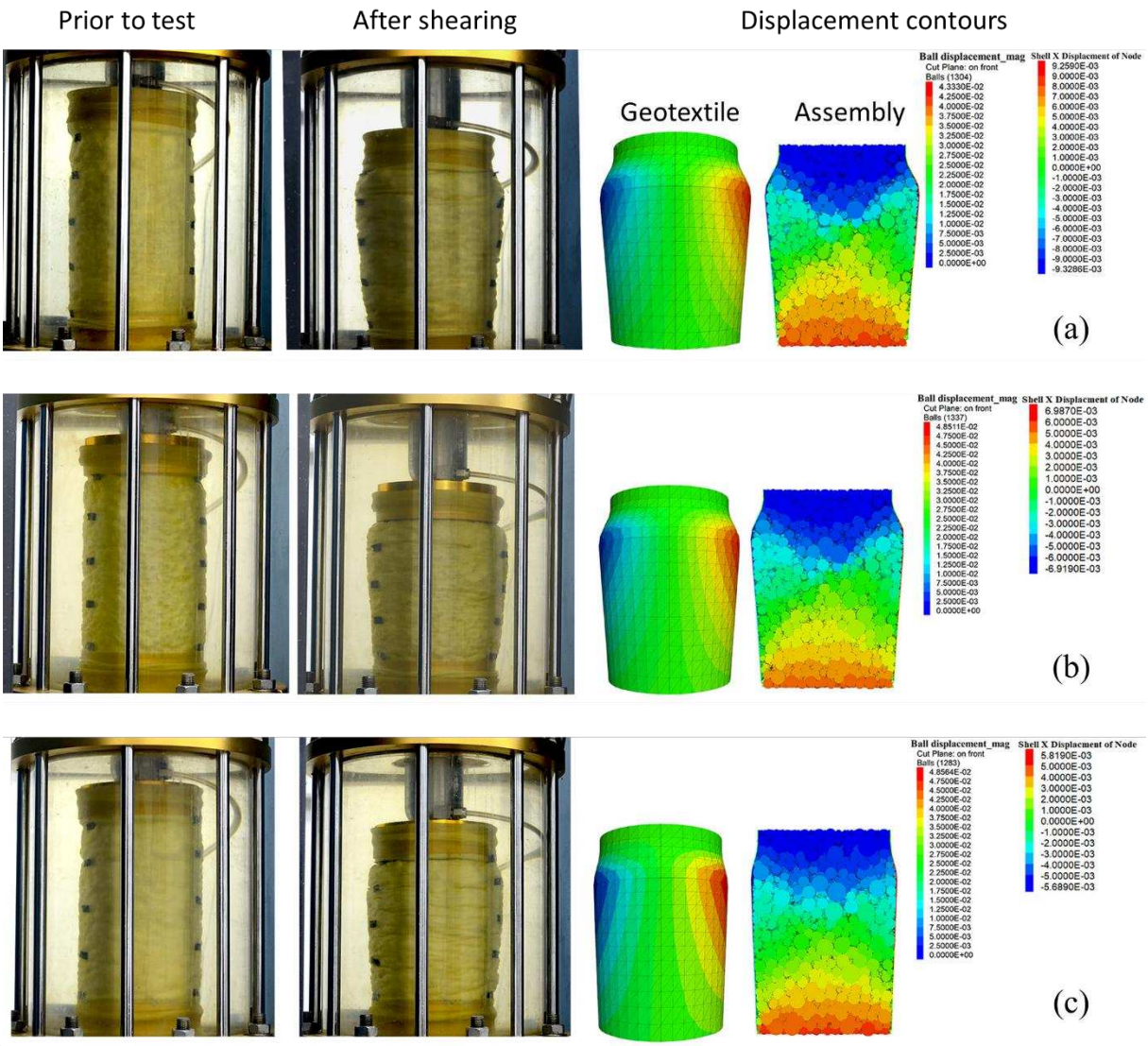

Figure 9. Comparison of deformations: laboratory tests vs. simulations at varying confining pressures: (a) 50 kPa; (b) 100 kPa; (c) 150 kPa

In summary, the numerical prediction model demonstrated consistency with the triaxial test outcomes in terms of stress-strain curves and radial deformation of the column. Thus, it was concluded that the model was suitable for further mesomechanical analysis of encased cinder gravels, using the meso-parameters presented above.

3. Load-Deformation Mechanisms of a Single GECG Column

This section examines the loading-deformation behavior of GECG columns under a controlled, constant confining stress, building on existing research on uniaxial compression testing of GESC (Tan et al., 2020; Chen et al., 2018; Gniel and Bouazza, 2010; Gu et al., 2017a; Gu et al., 2017b; Gu et al., 2023). The DEM-FDM model validated in Section 2 serves to explore the compression and load-bearing attributes of these

columns.

For subsequent numerical simulations, a confining stress of 50 kPa was applied. This choice was influenced by the model's ability to deform under lower vertical pressures, thereby optimizing computational efficiency. A length-to-diameter ratio of 5:1 was implemented in the numerical simulations, presenting a geometric configuration challenging to examine through laboratory triaxial compression tests. Although Gu et al. (2023) studied the unconfined compressive behavior of GECG columns with this specific length-to-diameter ratio, their behavior under a constant, controlled confining stress has not yet been investigated.

The analysis proceeds with a mesomechanical investigation, aimed at refining the design theory for GECG columns. This involves scrutinizing both their macroscopic load-deformation characteristics and mesoscopic-scale mechanical responses. All other parameters and conditions align with those outlined in Section 2.

3.1 Compression Behavior and Load-Bearing Capacity of the Column

Figure 10 illustrates the modelling domain for a single GECG column with a diameter of 100 mm and a length of 500 mm. The parameters for the geotextile and cinder gravel particles are consistent with those elucidated in Section 2. In order to optimize computational efficiency, adjustments were made to the gradation of the assembly, with 20% of the mass attributed to grain sizes ranging from 10 to 15 mm, 67% for grain sizes between 5 to 10 mm, and 13% for grain sizes spanning 2 to 5 mm. During the shearing phase, the upper wall remains stationary, while the lower wall compresses the specimen at a rate of 6×10^{-7} m/s. Real-time data is recorded for the displacement and average stress experienced by both the upper and lower walls throughout the testing process. The measurement system incorporates nine spheres, each with an 80 mm diameter, arranged from the top to the base, with each sphere encompassing a minimum of 2,000 particles.

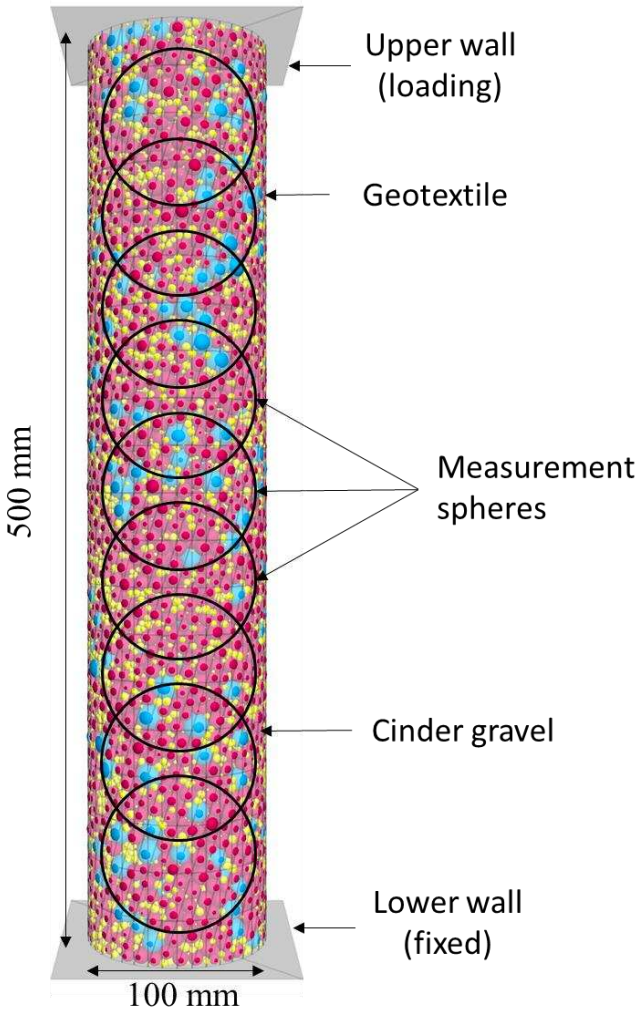

Figure 10. Schematic of a single simulated GECG column under triaxial compression

Figure 11a illustrates the relationship between vertical pressure and displacement of the GECG column. During the initial loading phase, the vertical pressure-displacement curve exhibits a nonlinear increase, with the column quickly reaching 120 kPa at minimal vertical displacement. As the pressure continues to increase, the column's behavior demonstrates softening, accompanied by a steady increase in vertical displacement and a gradual decrease in the rate of stress growth. When the vertical displacement exceeds 10 mm, the column undergoes significant nonlinear deformation. Upon achieving a top pressure of 276 kPa, the top vertical displacement progresses rapidly, and the pressure-displacement curve nearing a vertical gradient, indicating that the column has reached its bearing capacity.

Under the influence of the applied load, the GECG column experiences radial deformation. The distribution of radial deformation along the column shaft not only indicates the effective length of load transmission but also

dictates the bearing capacity and failure mechanism of the GECG column. Figure 11b portrays the expansion of the column at various stages of vertical displacement. The expansion at different heights increase with the vertical displacement. The maximum expansion is restricted within 2 times the column diameter (represented as 2D), with peak expansion occurring at 1.5D.

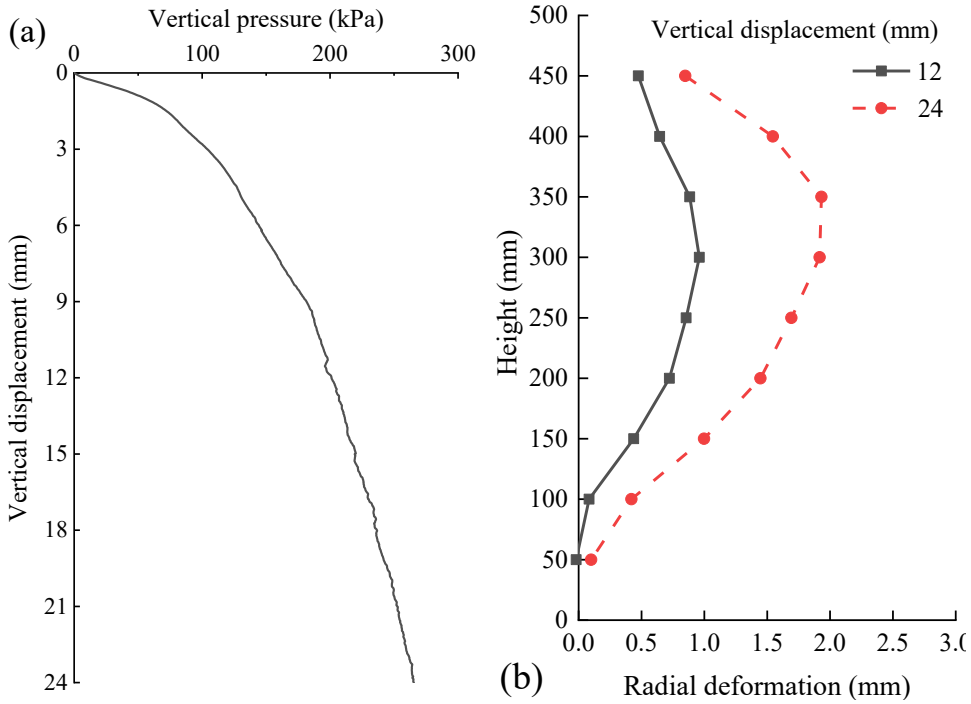

Figure 11. Vertical pressure-displacement curve (a) and radial deformation distributions (b) along the height

3.2 Mesoscopic Analysis of Cinder Gravel Assemblies

Figure 12a illustrates the vertical stress distribution in cinder gravel particles along the shaft. Vertical stress at varying heights was calculated as the average vertical stress within the corresponding position's measuring sphere. The vertical stress distribution along the shaft showed a diverse pattern under different axial strains. During the initial loading phase, at a vertical displacement of 12 mm, the vertical stresses across different positions were similar, indicating a uniform stress distribution throughout the column. At this stage, the column uniformly transferred the upward loading force along the shaft, thus demonstrating the bearing ability of the columns. This occurred because the geotextile sleeve had negligible radial deformation during initial loading. As loading continued, the vertical stress along the shaft increased with the growth in vertical displacement. Notably, there were larger increments in vertical stress near the top and base of the column. because these areas were in the vicinity of the upper and lower walls, which inhibited vertical particle displacement. Consequently, a higher particle contact force generated additional vertical stress.

Figure 12b highlights that the radial stress distribution along the shaft differed under various axial strains, with radial stress increasing as vertical displacement increased. During the initial loading stage, the radial stress distribution was similar across all heights; however, larger radial stresses occurred at the column top and base. This was again due to the fixed constraints at the top and base, which prohibited radial deformation within a certain vicinity, thus generating greater particle contact forces and additional radial stress. In the middle and lower sections of the column, the radial stress at various heights exhibited minimal changes and reduced values, indicating the geotextile had not fully exerted its constraining effect at these locations.

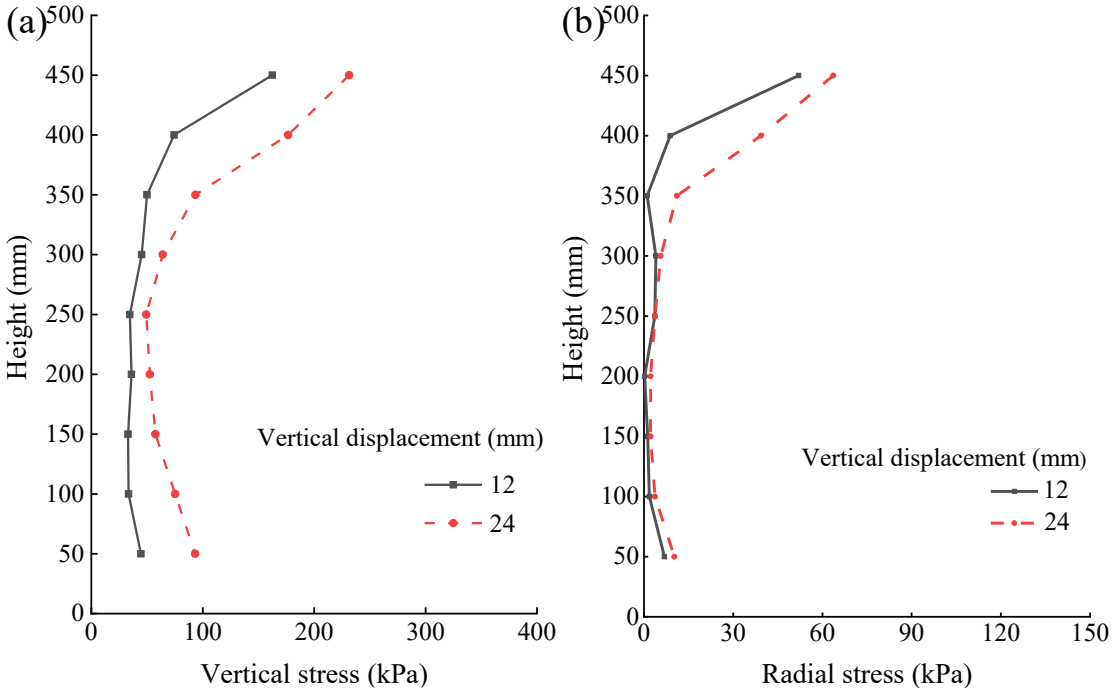

Figure 12. Stress distribution within cinder gravel assemblies along height: (a) vertical; (b) radial

Figure 13 presents the distribution of contact forces within the GECG column. The contact forces are represented by scattered bars, with the bar thickness correlating with the contact force magnitude. Due to the vast number of particles, there is a corresponding large number of contact forces. Thus, contact forces below 5 N were disregarded for observation purposes. Figure 13a displays the contact force contour before and after loading, with the maximum contact force being 74.4 N prior to loading and evenly distributed across different heights. After loading, the contact force reached 94.2 N. These force chains interconnected and dispersed in a crisscross pattern, forming a force chain network structure. As these particles directly supported the vertical load, the largest contact forces were distributed at the interface between the particles and the upper wall. During the shearing process, the contact forces between particles underwent continuous disruption and reorganization. With the increase in axial strain, the assembly densification increased, and the contact forces rose accordingly,

manifesting as increased stressed near the top of the column.

Figure 13b displays the force chain networks within the column, illustrating the distribution of the contact forces of varying magnitudes, with the minimum visible contact forces set at 20 N, 40 N, and 60 N. Few contact forces exceeded 60 N, and those that did, represent strong force chains primarily distributed near the upper section of the column and adjacent to the loading wall. Contact forces above 40 N were predominantly distributed in the upper-middle region, though their total numbers remained limited. In contrast, the majority were contact forces above 20 N, which acted as the secondary force chain network and displayed a relatively uniform distribution. Predominantly vertical force chains characterized the contact forces, with comparatively fewer horizontal force chains, resulting in lower radial stresses compared to vertical stress. The distribution of the force chain networks at various locations corresponded to the vertical and radial stresses at different positions. Moreover, the force chain distribution in the longer columns aligned with that of the triaxial test specimens.

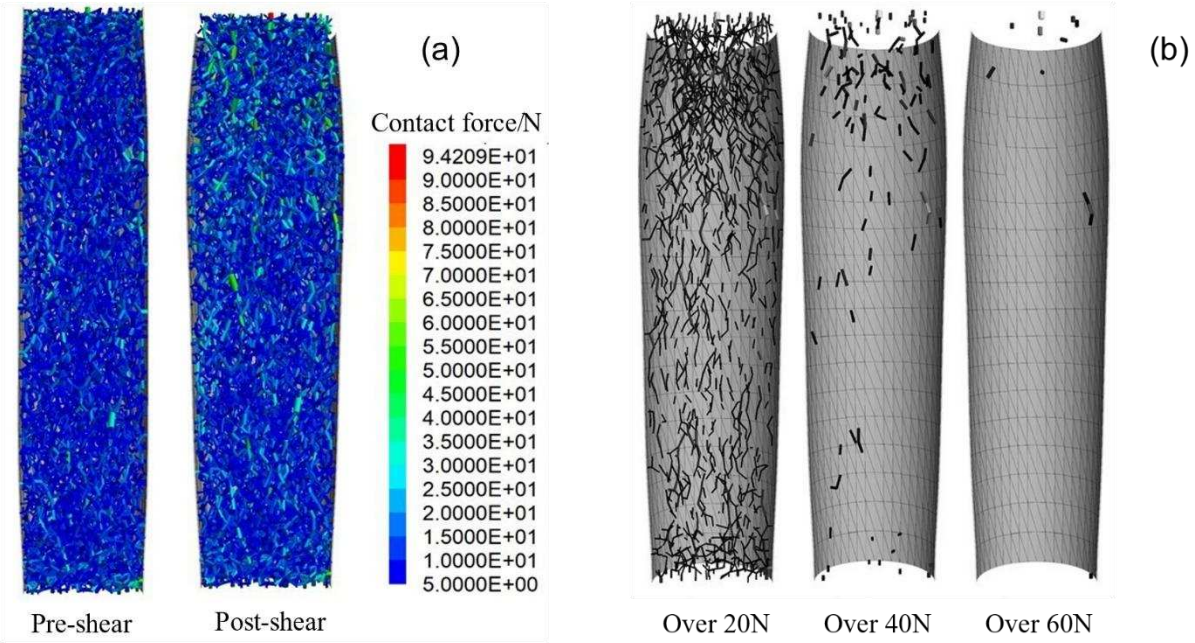

Figure 13. (a) Contact force contours and (b) distributions at varying thresholds

Figure 14a and Figure 14b depict the variation in porosity with column vertical displacement and height, respectively. Under a confining pressure of 50 kPa, the initial porosity ranged from 0.22 to 0.26. Following the commencement of loading, porosity slightly decreased within 100 mm of the top and base of the column as the assembly gradually compacted under the movement of the loading plate. In the middle of the column, which is away from the upper and lower wall, the granules largely maintained their original contact state during loading,

without generating significant contact forces. The pores between particles remained relatively large, the geotextile exhibited expansion deformation, and porosity gradually increased.

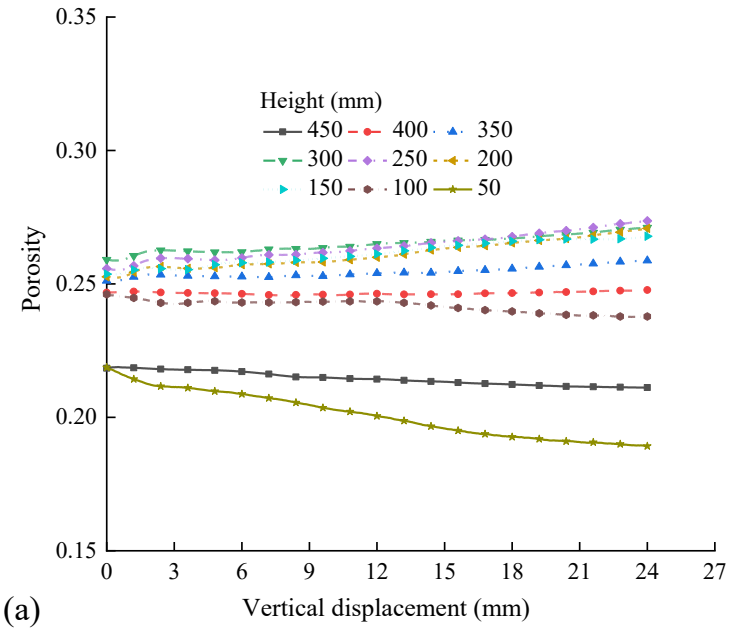

(a)

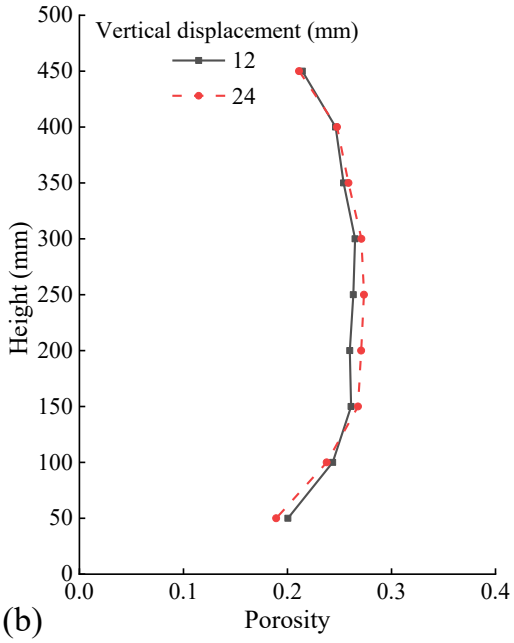

(b)

Figure 14. Porosity variations in cinder gravel assemblies: (a) with vertical displacement; (b) with height

Figures 15a and 15b show the variation in coordination number with column vertical displacement and height, respectively. Coordination number is a mesoscopic parameter where a higher coordination number typically indicates a more stable and compact particle state. The initial coordination number of the particles ranged between 4 and 5, suggesting each particle was in contact with an average of 4 to 5 other particles, transmitting contact forces, and the assembly was in a stable state to effectively transfer inter-particle contact

forces. During the loading phase, the coordination number slightly increased within a 100 mm range at the top and base of the column, signifying a compaction process in the upper and lower sections of the pile. Conversely, the coordination number in the middle section decreased with increasing head load, resulting in a decline in overall particle compaction. The coordination number variation at different heights aligned with changes in porosity, reflecting the relative density of the cinder gravel particles. When the column was compressed, the coordination number showed that the upper and lower portions became more compacted while the middle portion became less dense.

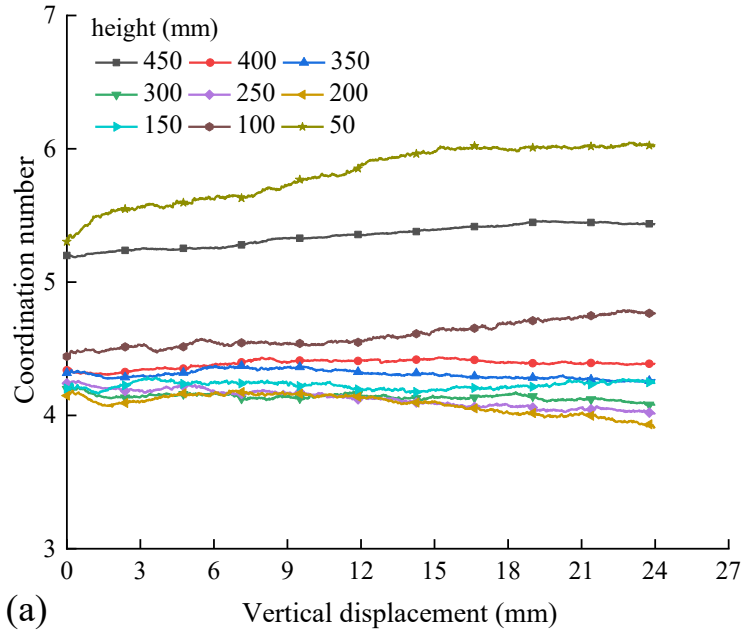

(a)

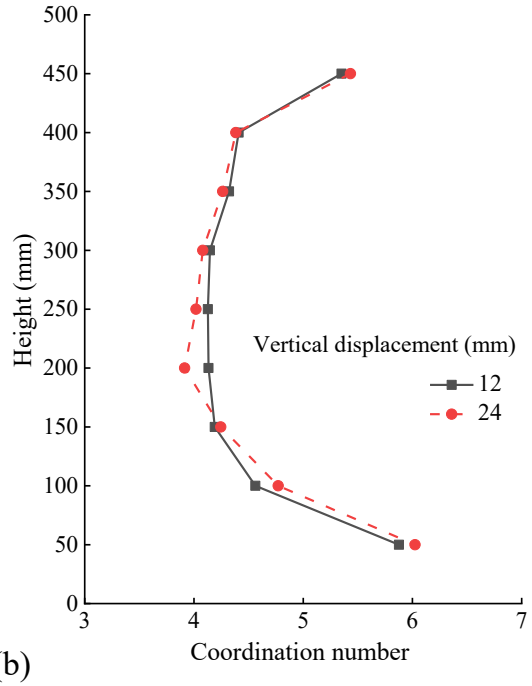

(b)

Figure 15. Coordination number variations in cinder gravel assemblies: (a) with vertical displacement; (b) with height

4. Parametric Study

This section conducts a parametric analysis centered on two key parameters: relative density and gradation of the assemblies. Table 6 outlines six levels of relative density (0.4, 0.5, ..., 0.9) and three different gradations (S2, S3, S4). These relative densities are further characterized by corresponding porosity values, serving as mesoscopic parameters in the DEM. Table 7 details the properties of three samples with varying gradations.

Table 6. Simulation metrics for GECG columns

Group ID	ID	Column Length (mm)	Column diameter (mm)	Relative density (%)	Gradation
1. Relative density	1	500	100	40 (n=0.417)	S1
	2	500	100	50 (n=0.413)	S1
	3	500	100	60 (n=0.409)	S1
	4	500	100	70 (n=0.405)	S1
	5	500	100	80 (n=0.400)	S1
	6	500	100	90 (n=0.397)	S1
	7	500	100	80 (n=0.4)	S2
	8	500	100	80 (n=0.4)	S3
	9	500	100	80 (n=0.4)	S4

Note: Details for S2, S3, and S4 are elaborated in Table 7; n denotes the porosity.

Table 7. Gradation characteristics and meso-parameters of selected assemblies

Sample ID	S2	S3	S4
P_{10} (%)	40	60	80
d_{10}	2.5	2.2	2.1
d_{30}	6.3	7.4	10.9
d_{60}	10.0	12.6	14.2
C_u	4.0	5.7	6.8
C_c	1.6	2.0	4.0
Contact effective modulus ($\times 10^{-6}$)	7.2	7.5	8.25
Normal-to-tangential stiffness ratio	3.5	3.5	2.9
Interparticle friction coefficient	0.5	0.5	0.5

Note: P_{10} refers to the percent by mass for grain size between 10 and 20 mm. The contact effective modulus, normal-to-tangential stiffness ratio, and interparticle friction coefficient have been calibrated.

4.1 Impact of Relative Density

This section explores the influence of the relative density by adjusting porosity. Figure 16 presents the vertical pressure-displacement curves for different relative density. During the initial loading phase, the vertical pressure at the top of the column increased linearly with vertical displacement. Upon reaching a vertical displacement of 5mm, columns with a relative density exceeding 0.7 displayed rapid nonlinear behavior. After reaching a certain

displacement threshold, the vertical pressure-displacement curves for columns with relative densities of 0.8, and 0.9 became nearly vertical, signifying that the columns had reached its ultimate bearing capacity. In contrast, columns with relative densities below 0.8 exhibited linear pressure increases with displacement within the observed range, without reaching their ultimate bearing capacity. Increasing the relative density resulted in enhanced column strength. In columns with a relative density of 0.9, an increase in vertical pressure led to a rearrangement of particles, which resulted in a rapid increase in vertical strain when the vertical displacement exceeded 15mm.

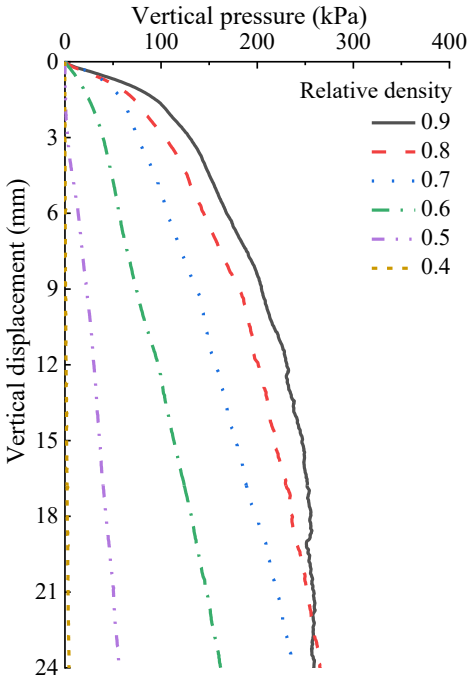

Figure 16. Vertical pressure-displacement curves for GECG columns at different relative densities

Figure 17 illustrates the distribution of radial expansion along the height of GECG columns as column vertical displacement develops, with varying relative densities. During the initial loading phase, columns displayed almost no apparent radial deformation, while radial shrinkage was observed throughout the entire column for relative densities of 0.5 and 0.4. This phenomenon arose due to low relative densities impeding normal particle contact upon loading, resulting in reduced contact forces and geosynthetic shrinkage under circumferential pressure. As loading increased, the radial deformation of the geosynthetic material increased, revealing consistent expansion deformation patterns in the columns with a relative density of 0.6 and above. In contrast, the columns with relative densities of 0.5 and 0.4 continued to experience shrinkage in the lower-middle portion of the geosynthetic material.

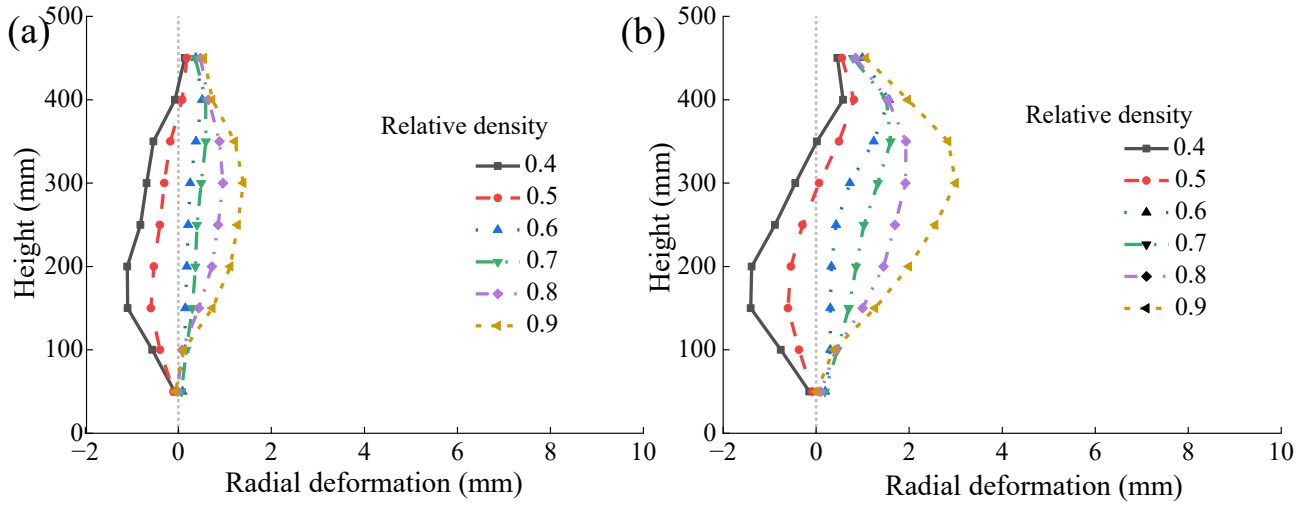

Figure 17. Radial deformation-height curves at various relative densities: (a) 12 mm; (b) 24 mm

4.2 Effect of Cinder Gravel Gradation

Figure 18 displays the vertical pressure-displacement curves for GECG columns with various aggregate gradations. In the phase of minimal vertical displacement, the vertical pressure increased linearly with the vertical displacement for different gradations, and the variation in vertical pressure among different gradations was negligible. However, as the load intensified, discrepancies emerged in the vertical pressure-displacement characteristic of columns with various gradations. At a vertical displacement of 24mm, the measured pressures were 228.5 kPa, 239.4 kPa, and 248.7 kPa for S2, S3 and S4, respectively. This increase in pressure corresponded to a successive escalation in the percent by mass for grain sizes ranging from 10 to 20 mm in S2 to S4. This suggests that the higher content of coarse particles in the gradation enhanced the bearing capacity of the GECG columns.

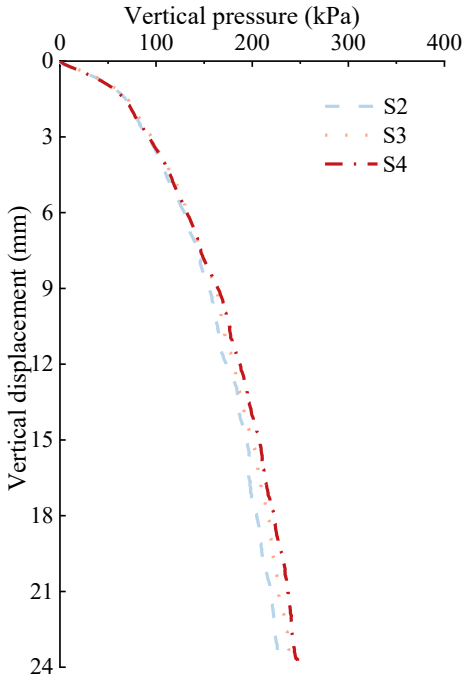

Figure 18. Vertical pressure-displacement curves for GECG columns with different fill gradations

Figure 19 portrays the distribution of radial expansion of geotextiles with height for different column vertical displacements and aggregate gradations. During the initial loading phase, radial deformation in various columns was relatively minor, and differences were negligible. As loading increased, radial deformation of the geotextiles also increased. The distribution pattern of radial expansion with height exhibits pronounced expansion deformation within the range of 1D to 2D from the top. In this stage, the maximum expansion deformation for S2, S3 and S4 were 1.95mm, 2.16mm and 2.34mm, illustrating that the higher the coarse particle content the larger the maximum expansion. Furthermore, the larger radial deformation of the geotextiles in the columns showed a more effective utilization of the enveloping effect, correlating with an increased bearing capacity as shown in the Figure 18.

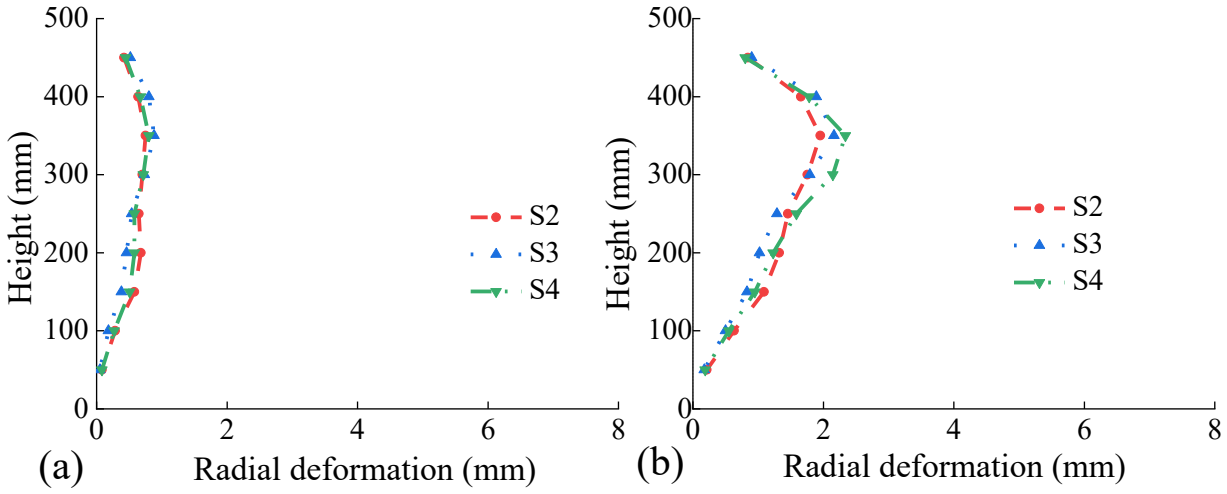

Figure 19. Radial deformation-height curves at varying gradations: (a) 12 mm; (b) 24 mm

This study explored the behavior of geotextile-encased cinder gravel columns subjected to triaxial compression through a coupled DEM-FDM model. It's important to note that the cinder gravel would prone to particle breakage when subject to the load. Although preliminary measures such as the screening of fragile particles prior to testing have been implemented, these do not fully resolve breakage issues. Therefore, it is better to incorporate the simulation of particle breakage within the DEM model. Given the complexity of cinder gravel breakage, further laboratory experiments and numerical simulations are essential. These, however, are beyond the scope of this paper and are considered for future research.

5. Conclusions

This study conducted consolidated drained triaxial tests on cinder gravel specimens, both with and without geotextile encasement. Two DEM models were then developed to replicate the laboratory tests. The goal was to identify both macro- and meso-parameters by comparing stress and strain with test results. For specimens with geotextile encasement, a triaxial test model for encased cinder gravel was created using a combined DEM-FDM approach. Validation of this model entailed matching stress-strain relationships, radial expansion behavior, and deformation contours of the column with laboratory test results under varying confining pressures.

The parametric analysis of GECG columns, featuring larger aspect ratios than lab-scale specimens, showed that most significant expansion occurred within the range of 1D to 2D from the top of the column. In contrast, the column's central and lower regions experienced minimal expansion. This suggests that geotextile encasement at these heights does not fully optimize its confining effect. In the areas of expansion, particle contact forces rose substantially, and the formation of robust force chains moved downward, corresponding with increased vertical displacement in the column.

Variations in porosity and coordination number indicated a gradual increase in compactness in both the upper and lower sections of the column during loading. This was contrasted with a minor decrease in compactness in the midsection. Keeping the column geometry constant, higher relative densities led to enhanced column strength. Additionally, an increased presence of coarse grains in the aggregate notably boosted the column's bearing capacity.

The study underscores the utility of GECG columns as a sustainable construction solution by investigating

their load-deformation mechanisms. Future research could aim to assess the performance of GECG column groups in enhancing soft ground conditions.

Acknowledgments

This study was supported by the National Natural Science Foundation of China under grant numbers 52078427 and 52078435, the Natural Science Foundation of Sichuan Province under grant number 2023NSFSC0391, and the 111 Project under grant number B21011.

References

Abu-Farsakh, M., Coronel, J. & Tao, M. (2007). Effect of soil moisture content and dry density on cohesive soil–geosynthetic interactions using large direct shear tests. *Journal of Materials in Civil Engineering,* 19, No. 7, 540-549.https://doi.org/10.1061/(ASCE)0899-1561(2007)19:7(540)

Bai, Y., Li, X., Yang, W., Xu, Z. & Lv, M. (2022). Multiscale analysis of tunnel surrounding rock disturbance: A PFC3D-FLAC3D coupling algorithm with the overlapping domain method. *Computers and Geotechnics,* 147, 104752. https://doi.org/10.1016/j.compgeo.2022.104752

Baral, P., Indraratna, B., Rujikiatkamjorn, C., Kelly, R. & Vincent P. (2021). Consolidation by Vertical Drains beneath a Circular Embankment under Surcharge and Vacuum Preloading. *Journal of Geotechnical and Geoenvironmental Engineering,* 147, No. 8, 05021004. https://doi.org/10.1061/(ASCE)GT.1943-5606.0002576

Cai, M., Kaiser, PK., Morioka, H., Minami, M., Maejima, T., Tasaka, Y. & Kurose, H. (2007). FLAC/PFC coupled numerical simulation of AE in large-scale underground excavations. *International Journal of Rock Mechanics and Mining Sciences,* 44, No. 4, 550-564. https://doi.org/10.1016/j.ijrmms.2006.09.013

Castro, J. (2017). Groups of encased stone columns: Influence of column length and arrangement. *Geotextiles and Geomembranes,* 45, No. 2, 68–80. https://doi.org/10.1016/j.geotexmem.2016.12.001

Chen, JF., Wang, XT., Xue, JF., Zeng, Y. & Feng SZ. (2018). Uniaxial compression behavior of geotextile encased stone columns. *Geotextiles and Geomembranes*, 46, No. 3, 277-283. https://doi.org/10.1016/j.geotexmem.2018.01.003

Chen, JF., Li, LY., Zhang, Z., Zhang, X., Xu, C., Rajesh, S. & Feng, SZ. (2021). Centrifuge modeling of geosynthetic-encased stone column-supported embankment over soft clay. *Geotextiles and Geomembranes,* 49, No. 1, 210–221. https://doi.org/10.1016/j.geotexmem.2020.10.021

Connolly, DP., Dong, K., Alves Costa, P., Soares, P. & Woodward, PK. (2020). High speed railway ground dynamics: a multi-model analysis. *International Journal of Rail Transportation,* 8, No. 4, 324–346. https://doi.org/10.1080/23248378.2020.1712267

Cui, X., Li, X., Du, Y., Bao, Z., Zhang, X., Hao, J., Hu, Y. (2024) Macro-micro numerical analysis of granular materials

558 considering principal stress rotation based on DEM simulation of dynamic hollow cylinder test. *Construction and Building*
559 *Materials*, 412, 134818. https://doi.org/10.1016/j.conbuildmat.2023.134818
560 Debnath, P. & Dey, AK. (2017). Bearing capacity of geogrid reinforced sand over encased stone columns in soft clay.
561 *Geotextiles and Geomembranes,* 45, No. 6, 653–664. https://doi.org/10.1016/j.geotexmem.2017.08.006
562 Feng, G., Luo, Q., Wang, T., Connolly, D.P., Liu, K. (2024) Frequency Spectra Analysis of Vertical Stress in Ballasted Track
563 Foundations: Influence of Train Configuration and Subgrade Depth. *Transportation Geotechnics*, 44, 101167.
564 https://doi.org/10.1016/j.trgeo.2023.101167
565 Gniel, J. & Bouazza, A. (2010). Construction of geogrid encased stone columns: A new proposal based on laboratory testing.
566 *Geotextiles and Geomembranes*, 28, No. 1, 108-118. https://doi.org/10.1016/j.geotexmem.2009.12.012
567 Gu, M., Han, J. & Zhao, M. (2017a). Three-Dimensional Discrete-Element Method Analysis of Stresses and Deformations
568 of a Single Geogrid-Encased Stone Column. *International Journal of Geomechanics,* 17, No. 9, 04017070.
569 https://doi.org/10.1061/(ASCE)GM.1943-5622.0000952
570 Gu, M., Han, J. & Zhao, M. (2017b). Three-dimensional DEM analysis of single geogrid-encased stone columns under
571 unconfined compression: a parametric study. *Acta Geotechnica*, 12, No. 3, 559-572. https://doi.org/10.1007/s11440-
572 017-0547-z
573 Gu, M., Zhao, M., Zhang, L. & Han, J. (2016). Effects of geogrid encasement on lateral and vertical deformations of stone
574 columns in model tests. *Geosynthetics International,* 23, No. 2, 100–112. https://doi.org/10.1680/jgein.15.00035
575 Gu, M., Cai, X., Mo, H. & Wang, Q. (2023). Unconfined compressive behavior of column with geogrid-encased recycled
576 aggregate: Test and simulation. *Construction and Building Materials,* 400, 132528.
577 https://doi.org/10.1016/j.conbuildmat.2023.132528
578 Hearn, GJ., Otto, A., Greening, PAK., Endale, AA. & Etefa, DM. (2019). Engineering geology of cinder gravel in Ethiopia:
579 prospecting, testing and application to low-volume roads. *Bulletin of Engineering Geology and the Environment,* 78,
580 3095–3110. https://doi.org/10.1007/s10064-018-1333-3
581 Hong, YS., Wu, CS. & Yu, YS. (2016). Model tests on geotextile-encased granular columns under 1-g and undrained
582 conditions. *Geotextiles and Geomembranes,* 44, No. 1, 13–27. https://doi.org/10.1016/j.geotexmem.2015.06.006
583 Huang, R. (2011) Research on Engineering Properties and Decision Model of Treatment Scheme of Soft Soil of Sichuan
584 Basin. Southwest Jiaotong University, Chengdu.
585 Jia, M., Yang, Y., Liu, B. & Wu, S. (2018). PFC/FLAC coupled simulation of dynamic compaction in granular soils. *Granular*
586 *Matter,* 20, 1-15. https://doi.org/10.1007/s10035-018-0841-y
587 Kadhim, ST., Parsons, RL. & Han, J. (2018). Three-dimensional numerical analysis of individual geotextile-encased sand
588 columns with surrounding loose sand. *Geotextiles and Geomembranes,* 46, No. 6, 836–847.
589 https://doi.org/10.1016/j.geotexmem.2018.08.002

590 Kempfert, HG. & Raithel, M. (2005). Chapter 32 Soil improvement and foundation systems with encased columns and
591 reinforced bearing layers, in: Indraratna, B., Chu, J. (Eds.), Elsevier Geo-Engineering Book Series, Ground
592 Improvement — Case Histories. Elsevier, pp. 923–946. https://doi.org/10.1016/S1571-9960(05)80035-7
593 Keykhosropur, L., Soroush, A. & Imam, R. (2012). 3D numerical analyses of geosynthetic encased stone columns.
594 *Geotextiles and Geomembranes*, 35, 61-68.
595 Liu, H., Luo, Q,. El Naggar, M.H., Zhang, L. & Wang, TF. (2023). Centrifuge modeling of stability of embankment on soft soil
596 improved by rigid columns. *Journal of Geotechnical and Geoenvironmental* Engineering, 149, No. 9,
597 04023069.https://doi.org/10.1061/JGGEFK.GTENG-11314
598 Liu, K., Qiu, R., Yan, T., Wu, B., Fan, J., Yue, F. & Mei, G. (2022). Model test of clogging effects on composite foundation of
599 geosynthetic-encased steel slag column. *Geotextiles and Geomembranes*, 50, No. 5, 858-
600 867.https://doi.org/10.1016/j.geotexmem.2022.05.001
601 Liu, K., Qiu, R., Gou, J., Ning, B., Cui, C., Chen, Y. & Wang, T. (2024) Experimental and numerical exploration of a new
602 application of coal slag to treat loose sand foundation. *Journal of Cleaner Production*, 441, 140936.
603 https://doi.org/10.1016/j.jclepro.2024.140936
604 Luo, Q., Liang, D., Wang, T., Zhang, L. & Jiang, L. (2020). Application of High-Vesicularity Cinder Gravels to Railway Earth
605 Structure in Ethiopia. J*ournal of Materials in Civil Engineering,* 32, No. 11, 04020347.
606 https://doi.org/10.1061/(ASCE)MT.1943-5533.0003432
607 Ma, H., Luo, Q., Wang, T., Jiang, H. & Lu, Q. (2021). Numerical stability analysis of piled embankments reinforced with
608 ground beams. *Transportation Geotechnics,* 26, 100427. https://doi.org/10.1016/j.trgeo.2020.100427
609 Ministry of Housing and Urban-Rural Development of the PRC (2013) Technical code for ground treatment of buildings.
610 China Architecture Publishing & Media Co., Ltd, Beijing.
611 Miranda, M., Da Costa, A., Castro, J. & Sagaseta, C. (2017). Influence of geotextile encasement on the behaviour of stone
612 columns: Laboratory study. *Geotextiles and Geomembranes,* 45, No. 1, 14–22.
613 https://doi.org/10.1016/j.geotexmem.2016.08.004
614 Miranda, M., Da Costa, A., Castro, J. & Sagaseta, C. (2015). Influence of gravel density in the behaviour of soft soils
615 improved with stone columns. *Canadian Geotechnical Journal,* 52, No. 12, 1968–1980. https://doi.org/10.1139/cgj-
616 2014-0487
617 Murugesan, S. & Rajagopal, K. (2006). Geosynthetic-encased stone columns: Numerical evaluation. *Geotextiles and*
618 *Geomembranes,* 24, No. 6, 349–358. https://doi.org/10.1016/j.geotexmem.2006.05.001
619 Nguyen, VD., Luo, Q., Wang, T., Liu, K., Zhang, L. & Nguyen, TP. (2023a). Load Transfer in Geosynthetic-Reinforced Piled
620 Embankments with a Triangular Arrangement of Piles. *Journal of Geotechnical and Geoenvironmental Engineering,*
621 149, No. 2, 04022131. https://doi.org/10.1061/JGGEFK.GTENG-10586

622 Nguyen, VD., Luo, Q., Wang, T., Zhang, L., Zhan, Y. & Nguyen, TP. (2023b). Monitoring of an instrumented geosynthetic-
623 reinforced piled embankment with a triangular pile configuration. *International Journal of Rail Transportation,* 11, No. 1,
624 69–91. https://doi.org/10.1080/23248378.2022.2032853
625 Ou, YangF., Zhang, JJ., Liao, WM., Han, JW., Tang, YL. & Bi, JB. (2017). Characteristics of the stress and deformation of
626 geosynthetic-encased stone column composite ground based on large-scale model tests. *Geosynthetics International,*
627 24, No. 3, 242–254. https://doi.org/10.1680/jgein.16.00028
628 Pandey, BK., Rajesh, S. & Chandra, S.(2022).Performance of Soft Clay Reinforced with Encased Stone Column: A
629 Systematic Review. *International Journal of Geosynthetics and Ground Engineering*, 8, No. 3, 40.
630 https://doi.org/10.1007/s40891-022-00387-x
631 Pandey, BK., Rajesh, S. & Chandra, S. (2021). Performance enhancement of encased stone column with conductive natural
632 geotextile under k0 stress condition. *Geotextiles and Geomembranes,* 49, No. 5, 1095–1106.
633 https://doi.org/10.1016/j.geotexmem.2021.03.004
634 Qu, T., Wang, S. & Hu, Q. (2019). Coupled discrete element-finite difference method for analyzing effects of cohesionless
635 soil conditioning on tunneling behaviour of EPB shield. *KSCE Journal of Civil Engineering,* 23, 4538-4552.
636 https://doi.org/10.1007/s12205-019-0473-8
637 Rajesh, S. (2017). Time-dependent behaviour of fully and partially penetrated geosynthetic encased stone columns.
638 *Geosynthetics International,* 24, No. 1, 60–71. https://doi.org/10.1680/jgein.16.00015
639 Tan, X., Hu, Z., Cao, M. & Chen, C. (2020). 3D discrete element simulation of a geotextile-encased stone column under
640 uniaxial compression testing. *Computers and Geotechnics*, 126, 103769.
641 https://doi.org/10.1016/j.compgeo.2020.103769
642 Tan, X., Hu, Z., Chen, C. & Zhao, M. (2021). 3D DEM-FDM Coupled Analysis of the Behavior of an Isolated Geogrid-
643 Encased Stone Column under Axial Loading. *Journal of Geotechnical and Geoenvironmental Engineering,* 147, No. 6,
644 04021028. https://doi.org/10.1061/(ASCE)GT.1943-5606.0002516
645 Tizpa, P., Chenari R, J. & Payan, M. (2023). PFC/FLAC 3D coupled numerical modeling of shallow foundations seated on
646 reinforced granular fill overlying clay with square void. *Computers and Geotechnics,* 161, 105574.
647 https://doi.org/10.1016/j.compgeo.2023.105574
648 Wang, T., Zhou, W., Chen, J., Xiao, X., Li, Y. & Zhao, X. (2014). Simulation of hydraulic fracturing using particle flow method
649 and application in a coal mine. *International Journal of Coal Geology,* 121, 1-13.
650 https://doi.org/10.1016/j.coal.2013.10.012
651 Wang, T., Chen, W., Li, T., Connolly, DP., Luo, Q., Liu, K. & Zhang, W. (2023a). Surrogate-assisted uncertainty modeling of
652 embankment settlement. *Computers and Geotechnics,* 159, 105498. https://doi.org/10.1016/j.compgeo.2023.105498
653 Wang, T., Luo, Q., Zhang, L., Xiao, S. & Fu, H. (2021). Dynamic response of stabilized cinder subgrade during train passage.

654 *Construction and Building Materials*, 270, 121370. https://doi.org/10.1016/j.conbuildmat.2020.121370
655 Wang, T., Ma, H., Liu, K., Luo, Q. & Xiao, S. (2022). Load transfer and performance evaluation of piled beam-supported
656 embankments. *Acta Geotech*, 17, No. 9, 4145–4171. https://doi.org/10.1007/s11440-022-01519-3
657 Wang, T., Nguyen, VD., Bui, PD., Luo, Q., Liu, K. & Zhang, L. (2023b). Three-dimensional physical modeling of load transfer
658 in basal reinforced embankments under differential settlement. *Geotextiles and Geomembranes,* 51, No. 2, 330–341.
659 https://doi.org/10.1016/j.geotexmem.2022.12.001
660 Xu, F., Moayedi, H., Foong, LK., Moghadam, MJ. & Zangeneh, M. (2021). Laboratory and numerical analysis of geogrid
661 encased stone columns. *Measurement,* 169, 108369. https://doi.org/10.1016/j.measurement.2020.108369
662 Yoo, C. & Abbas, Q. (2019). Performance of geosynthetic-encased stone column-improved soft clay under vertical cyclic
663 loading. *Soils and Foundations,* 59, No. 6, 1875–1890. https://doi.org/10.1016/j.sandf.2019.08.006
664 Zhang, L., Xu, Z., Zhao, H. & Zhou, S. (2021). A Three-Dimensional Discrete Element Modeling to Cyclic Response of
665 Geosynthetic-Encased Stone Column. *International Journal of Geosynthetics and Ground Engineering*, 7, 1–14.
666 https://doi.org/10.1007/s40891-021-00319-1
667 Zhang, L., Xu, Z. & Zhou, S. (2020). Vertical cyclic loading response of geosynthetic-encased stone column in soft clay.
668 *Geotextiles and Geomembranes,* 48, No. 6, 897–911. https://doi.org/10.1016/j.geotexmem.2020.07.006